Physiological homology between Drosophila melanogaster and vertebrate cardiovascular systems

Citation: Choma, M. A. et al. "Physiological Homology Between Drosophila Melanogaster and Vertebrate Cardiovascular Systems." Disease Models & Mechanisms 4.3 (2010): 411–420. Web.

As Published: http://dx.doi.org/10.1242/dmm.005231

Publisher: Company of Biologists Ltd.

Persistent URL: http://hdl.handle.net/1721.1/76783

Version: Final published version: final published article, as it appeared in a journal, conference proceedings, or other formally published context

Disease Models & Mechanisms 4, 411-420 (2011) doi:10.1242/dmm.005231

Physiological homology between *Drosophila melanogaster* and vertebrate cardiovascular systems

Michael A. Choma[1,2,3,*,‡], Melissa J. Suter[4,5], Benjamin J. Vakoc[4,5,6], Brett E. Bouma[4,5,6] and Guillermo J. Tearney[4,6,7]

SUMMARY

The physiology of the *Drosophila melanogaster* cardiovascular system remains poorly characterized compared with its vertebrate counterparts. Basic measures of physiological performance remain unknown. It also is unclear whether subtle physiological defects observed in the human cardiovascular system can be reproduced in *D. melanogaster*. Here we characterize the cardiovascular physiology of *D. melanogaster* in its pre-pupal stage by using high-speed dye angiography and optical coherence tomography. The heart has vigorous pulsatile contractions that drive intracardiac, aortic and extracellular-extravascular hemolymph flow. Several physiological measures, including weight-adjusted cardiac output, body-length-adjusted aortic velocities and intracardiac shear forces, are similar to those in the closed vertebrate cardiovascular systems, including that of humans. Extracellular-extravascular flow in the pre-pupal *D. melanogaster* circulation drives convection-limited fluid transport. To demonstrate homology in heart dysfunction, we showed that, at the pre-pupal stage, a troponin I mutant, *held-up2* (*hdp2*), has impaired systolic and diastolic heart wall velocities. Impaired heart wall velocities occur in the context of a non-dilated phenotype with a mildly depressed fractional shortening. We additionally derive receiver operating characteristic curves showing that heart wall velocity is a potentially powerful discriminator of systolic heart dysfunction. Our results demonstrate physiological homology and support the use of *D. melanogaster* as an animal model of complex cardiovascular disease.

INTRODUCTION

Over the past decade there has been increasing interest in using the open cardiovascular system of *Drosophila melanogaster* as an animal model of human cardiovascular disease (Bier and Bodmer, 2004). The *D. melanogaster* cardiovascular system (Fig. 1A) is open because it lacks discrete, closed return vasculature (Vogel, 1993). Vertebrates, by contrast, have a well-developed system of return vasculature represented by the venous tree. Previous research has demonstrated genetic, molecular, cellular and tissue function homology between the *D. melanogaster* and vertebrate cardiovascular systems. However, the degree of global physiological homology remains an open question. For example, it is unclear whether commonly measured physiological parameters such as cardiac output and aortic velocity, when normalized to measures of body size, are similar between *D. melanogaster* and important vertebrate species, including humans. Normalization can provide a basis for comparison across different size scales in addition to providing meaningful measures of physiological performance. In both pediatric (Lock, 2006) and adult (Kern and King, 2008) cardiology, it is standard practice to normalize cardiac output to body size to control for variation in cardiac output that is attributable to body size (Mohrman and Heller, 2006). In rodent (e.g. mouse, rat) cardiovascular research, it also is commonplace to normalize cardiac output to body size (e.g. Janssen et al., 2002; Slama et al., 2003). Aortic velocity normalized to body length provides a measure of global capacity for cardiac-driven, convection-limited transport of nutrients and signaling molecules across scales that are impractical for diffusion-mediated transport. Therefore, the comparison of normalized measures of cardiovascular performance among different species is a physiologically and metabolically relevant approach for establishing physiological homology.

The existence of cardiovascular physiological homology between vertebrates and *D. melanogaster* requires similarities not only in cardiovascular performance but also in cardiac-driven global mass transport dynamics. In vertebrates, an extensive vascular network provides for blood delivery throughout the body. Flow through this network is fast and mass transport in the vascular compartment is typically convection limited. In *D. melanogaster*, however, once hemolymph leaves the vascular compartment, delivery of hemolymph occurs throughout the body in an open manner in the extracellular-extravascular space. Therefore, convection-limited transport in *D. melanogaster* requires both rapid intravascular flow rates compared with body length as well as open return flow rates in the extracellular-extravascular compartment that can outpace diffusion-mediated transport. To date, these open mass transport dynamics are unknown and are often assumed to be slow (Kirby and Schachat, 2007).

In addition to basic measures of physiological performance, it is important to demonstrate that mutant *D. melanogaster* hearts can reproduce subtle functional heart defects that are observed

[1]Children's Hospital Boston, Boston, MA 02115, USA
[2]Department of Pediatrics, Harvard Medical School, Boston, MA 02115, USA
[3]Department of Diagnostic Radiology, Yale University School of Medicine, New Haven, CT 06520-8043, USA
[4]Wellman Center for Photomedicine, Massachusetts General Hospital, Boston, MA 02114, USA
[5]Department of Dermatology, Harvard Medical School, Boston, MA 02115, USA
[6]Harvard-MIT Division of Health Sciences and Technology, Cambridge, MA 02139, USA
[7]Department of Pathology, Harvard Medical School, Boston, MA 02115, USA
*Present address: Department of Diagnostic Radiology, Yale University School of Medicine, New Haven, CT 06520-8043, USA
‡Author for correspondence (michael.choma@yale.edu)

Received 3 January 2010; Accepted 28 October 2010

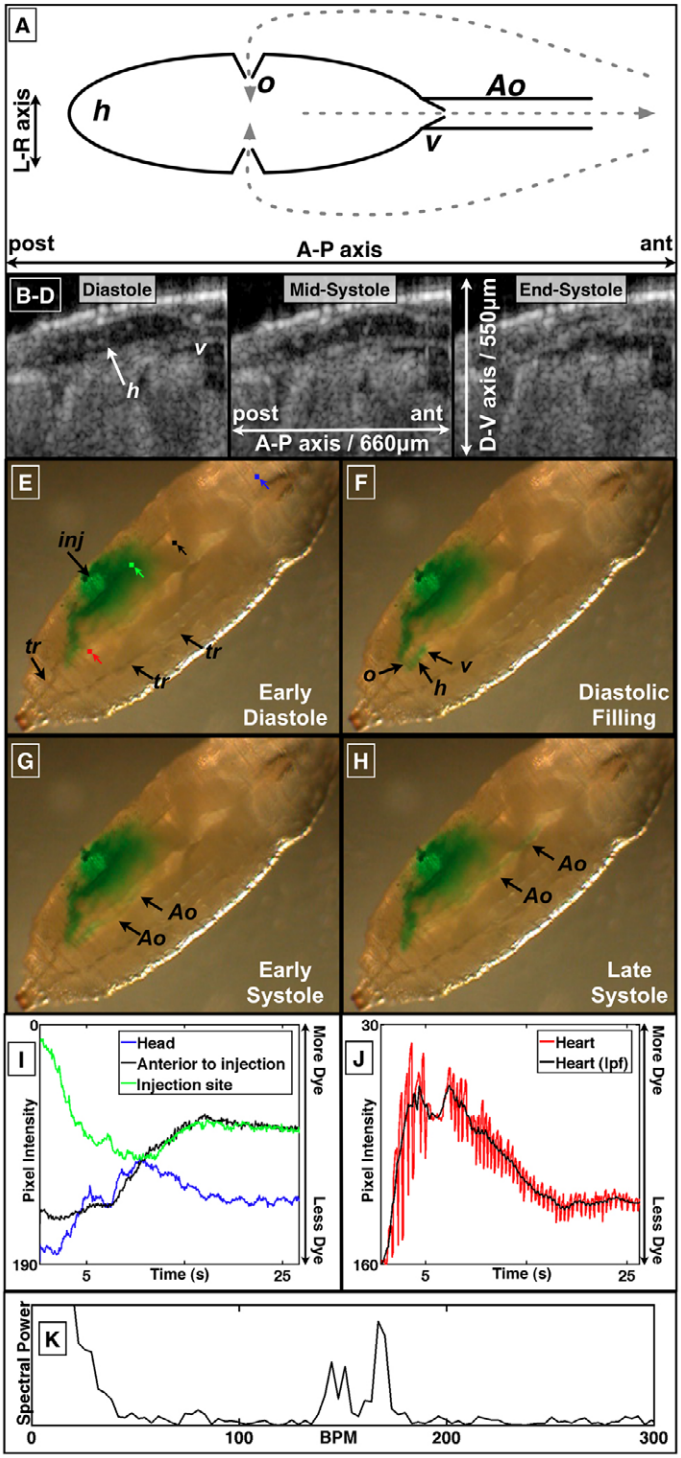

Fig. 1. Anatomic and functional imaging of the *D. melanogaster* cardiovascular system. (A) Schematic of an open circulatory system. Flow direction is indicated by dashed arrows. Cardiac cycle (B-H) in pre-pupal *D. melanogaster* images using sagittal plane OCT imaging (B-D; supplementary material Movie 1) and dye angiography (E-H; supplementary material Movie 2). (I,J) Time-varying pixel intensity at the color-coded landmarks in E. (K) Fourier transform of a segment of J, the time-varying heart pixel intensity. The peaks between 100 and 200 beats per minute (b.p.m.) are consistent with the pre-pupal heart rate. Ao, aorta; h, heart; inj, dye injection site; L, left; lpf, low pass filter; o, ostia; R, right; tr, trachea; v, valve.

clinically in humans. In particular, there is growing clinical interest in quantifying myocardial motion and function in terms other than pump efficiency (e.g. fractional shortening, ejection fraction) (Maeder and Kaye, 2009). In particular, there is a growing literature using local measures of myocardial function such as strain rate imaging (Yip et al., 2003; Marcucci et al., 2008) and Doppler-based measurements of heart wall velocity (Ho and Solomon, 2006; Marcucci et al., 2008; Maeder and Kaye, 2009). In addition, there is recent imaging work characterizing local myocardial function in diseased murine hearts (Pistner et al., 2010; Roy et al., 2010). Therefore, the relevance of *D. melanogaster* to human cardiovascular research would be enhanced if methods and mutants were available to demonstrate quantitative heart wall motion defects given their relevance to clinical medicine.

In this study, we demonstrated physiological homology between *D. melanogaster* and vertebrate cardiovascular physiology. Flow measurements were obtained using a novel dye angiography technique that allows for the real-time microscopic imaging of hemolymph flow in the open circulation of wild-type (OreR) pre-pupal *D. melanogaster*. The pre-pupal stage was chosen because: (1) the organism is relatively transparent, (2) it is stationary and does not require anesthesia or immobilization for imaging and (3) this stage represents the anatomic end-point of embryonic and larval development before entry into pupation. In conjunction with real-time structural and Doppler optical coherence tomography (OCT) (Huang et al., 1991; Vakoc et al., 2005; Choma et al., 2006; Wolf et al., 2006) imaging of the pre-pupal heart and aorta, we demonstrated that the open cardiovascular system of *D. melanogaster* has fast, cardiac-cycle-dependent, transport of hemolymph. Moreover, we found that several normalized measures of cardiovascular function, including cardiac output, aortic flow velocity and intracardiac flow velocity, were similar among *D. melanogaster*, humans and other vertebrates. We demonstrated that the *D. melanogaster* heart is a pulsatile pump that has intracardiac hemolymph velocities consistent with vertebrate embryo levels of intracardiac shear stress. We present evidence that convective mass transport can dominate over diffusive mass transport and that extracellular-extravascular flow is not isotropic but is partially directed. Finally, using a commercially available Doppler OCT system, we demonstrated impaired systolic and diastolic heart wall velocities in the pre-pupal, *held-up2* (*hdp2*) troponin I mutant (Beall and Fyrberg, 1991; Wolf et al., 2006); a finding made possible by detailed physiological phenotyping. Interestingly, heart wall velocity defects occur in the context of a non-dilated phenotype with only mildly depressed fractional shortening. Moreover, this finding complements a growing understanding that clinical heart failure can result from biomechanical defects in systolic and/or diastolic myocardial functioning, which require physiological characterization beyond ejection fraction assessment (Maeder and Kaye, 2009). Taken together, our results provide a physiological rationale for using *D. melanogaster* as an animal model of human cardiovascular disease, a rationale that is complementary to existing genetic and molecular evidence.

RESULTS

Cardiac physiology

We visualized the pre-pupal cardiac cycle using dye angiography and OCT (Fig. 1; supplementary material Movies 1, 2). From an

angiographic perspective, injection of dye adjacent to the heart allowed for characterization of several physiological aspects of the cardiac cycle. Systole was characterized by rapid ejection of dye out of the heart into the aorta and diastole by heart filling through the ostia (Fig. 1E-H; supplementary material Movie 1). There was rapid accumulation, then clearance of dye in the heart (Fig. 1J; supplementary material Movie 1). The accumulation and clearance dynamics are clearly evident in the low-pass-filtered version of the heart lumen pixel intensity signal (black curve in Fig. 1J) because the filtering minimizes beat-to-beat variability. Large beat-to-beat variability of intracardiac dye concentration was observed (Fig. 1J). The average periodicity of this variability corresponded well with the heart rate (Fig. 1K). Diastolic intake of hemolymph allowed for rapid clearance of injected extracellular-extravascular dye, whereas systolic ejection allowed for rapid transport of dye through the aorta and to the head (Fig. 1I and see below; supplementary material Movies 1 and 8). There was no observed retrograde flow from the aorta to the heart during diastole and diastolic filling, suggesting that this previously characterized anatomic valve (Curtis et al., 1999) does indeed function as a hemodynamic valve. These microangiographic findings were corroborated by OCT imaging of the heart-aorta junction (see below; supplementary material Movies 1 and 5). This junction opens at the onset of systole, indicating that pressure generated in the heart is very rapidly transmitted to the heart-aorta junction, resulting in the opening of the aortic valve. Moreover, there was closure of the aortic valve at the end of systole when forward flow falls to zero and cardiac pressure equilibrates with that in the extracellular-extravascular space.

We obtained echocardiographic parameters of the heart using OCT imaging. In the sagittal plane (n=5 organisms), the average diastolic long (anterior-posterior) and short (dorsal-ventral) axis diameters were 427±33 μm (mean ± s.d.) and 95±6.6 μm, respectively. The average heart rate was 135±23 beats per minute. Assuming a prolate spheroid model of the heart, we calculated an average end-diastolic volume (V_{ED}) of 2.0±0.3 nL ($V_{ED}=4/3\pi a^2 b$; a, short-axis radius; b, long-axis radius). Fractional shortening (i.e. percentage change from diastolic diameter during systole) of the short-axis of the anterior and posterior aspects of the heart were 82±26% and 93±16%, respectively. We did not observe shortening of the long-axis of the heart, consistent with previous histological observations that muscle fibers run only circumferentially and not longitudinally in P1 pupae (Curtis et al., 1999). Using a conservative estimate of a 75% ejection fraction, and assuming a pre-pupal body mass of 2 mg (Folk et al., 2001), we estimated a cardiac output normalized to body mass of 100 ml/minute/kg. For comparison, the normalized cardiac output in humans is ~70 ml/minute/kg assuming a heart rate of 80 beats per minute, a stroke volume of ~100 ml (Lang et al., 2005), an ejection fraction of ~60% (Lang et al., 2005), and a weight of ~70 kg (Kuczmarski et al., 2000); in dogs, ~150 ml/minute/kg (Berne and Levy, 1950); in 2 day post-fertilization (d.p.f.) zebrafish embryos, ~30 ml/minute/kg (Malone et al., 2007) assuming a weight of 700 μg (Hu et al., 2000); and in 5 d.p.f. zebrafish embryos, ~30 ml/minute/kg (Malone et al., 2007) assuming a weight of 1.2 mg (Hu et al., 2000). Weight-adjusted cardiac output in the mouse appears to be higher than that of pre-pupal *D. melanogaster*, but there is enormous variability in this measure in the literature (Janssen et al., 2002) (209-1300 ml/minute/kg). In terms of previous measurements in open circulations, the cockroach cardiac output can been estimated to be in the ~100 ml/minute/kg range (Birchard and Arendse, 2001) and several molluscs and arthropods have estimated cardiac outputs in the ~100 ml/minute/kg range (D. D. Jorgensen, Cardiac output and its distribution in the intertidal mollusc, *Haliotis cracherodii*, PhD thesis, Iowa State University, 1981).

Intracardiac shear rates and forces

We used M-mode Doppler OCT to measure early-systolic intracardiac flow velocities. We measured flow velocities by imaging individual hemocytes (i.e. blood cells) as they underwent acceleration during the early moments of systole (Fig. 2). We calculated intracardiac velocities on the order of one body length per second (~2-4 mm/second). This method underestimated peak hemocyte velocity because an individual hemocyte leaves the M-mode field of view before reaching peak velocity. Moreover, the hemocytes are not necessarily located in the mid-lumen, another factor that can underestimate flow velocity. For comparison, human blood velocities at the mitral and tricuspid valves are in the order of 0.6-1.3 m/second and 0.3-0.7 m/second, respectively (DeMaria and Blanchard, 2007), both of which are less than one body length per second (adult human body length is ~1.7 m) (Kuczmarski et al., 2000). Assuming that hemolymph flow in the *D. melanogaster* heart is viscous and non-turbulent, and assuming that there is insufficient time for a parabolic flow profile to develop, the shear

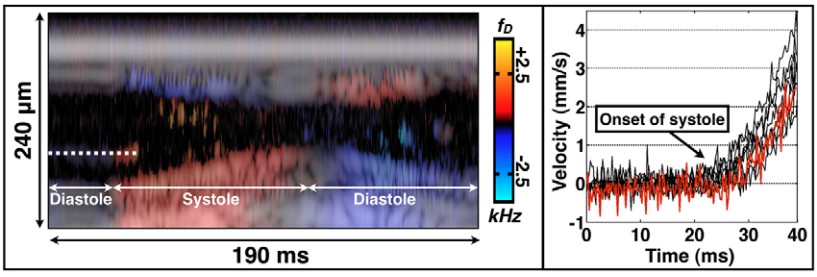

Fig. 2. Doppler velocimetry of heart wall motion and intracardiac hemocyte flow. The left panel is an M-mode Doppler/structural image during systole and diastole. The dashed line covers an individual hemocyte that undergoes marked acceleration at the initiation of systole. An accelerating hemocyte could be tracked for ~10 milliseconds before it exited the field of view of the M-mode line. The right panel is a velocity plot of eight individual hemocytes during distinct cardiac cycles (n=5 organisms). Hemocyte velocity from the dashed line in the left panel is shown in the red line. Hemocyte acceleration was ~0.2-0.3 m/second^2.

rate can be estimated from the quotient of the midline velocity and the vessel radius (Hove et al., 2003), yielding shear rates of ~40-60 second^{-1}. Since the Reynolds number (N_R) of pre-pupal intracardiac flow is ~0.1 ($N_R=\rho v d \mu^{-1}$; ρ, fluid density; v, fluid velocity; d, vessel diameter; μ, fluid viscosity), the viscous, non-turbulent assumption is valid. These shear rates are comparable to those in a 37 hour post-fertilization (h.p.f.) zebrafish embryo (Hove et al., 2003).

There are several reasons to assume that intracardiac flow profiles are not necessarily parabolic. First, immediately before the onset of systole, there is no flow in the heart, so the flow profile is flat. Even if the intracardiac flow profile develops into a parabolic shape during mid or late systole, the profile cannot immediately transition from flat to parabolic at the onset of systole. Second, the derivation of the governing equations for parabolic Hagen-Poiseuille flow (Papanastasiou et al., 2000) makes several assumptions that are violated in our experiments. Hagen-Poiseuille flow assumes steady-state flow (i.e. no flow velocity changes with respect to time) under a constant driving pressure and constant vessel diameter. These assumptions cannot be plausibly made during active systolic heart contraction. Third, from a microfluidics perspective, the time needed to dissipate unsteady inertial forces is $\tau_i \sim \rho d^2 \mu^{-1}$ (Squires and Quake, 2005). Using parameters described in this section, τ_i~4 milliseconds. Fig. 2 demonstrates that flow and wall motion time constants are shorter than τ_i, which also makes a quasi-steady-state assumption of well-developed flow challenging. In sum, our assumption of a linear flow profile in calculating shear rates provides a first-order, lower-limit estimate with the minimal assumptions that (1) the flow profile peak is midline and (2) higher-order flow profile shape (e.g. parabolic) will yield shear estimates that are higher, not lower, than the linear estimate. It also should be noted that these calculations are relevant to flow dynamics in vertebrate embryo hearts (e.g. human, zebrafish, *Xenopus*) with size scales of ~100 μm.

The constant of proportionality between shear rate and shear stress is dynamic viscosity. Unfortunately, the dynamic viscosity of *D. melanogaster* hemolymph has not been characterized. However, after assuming that the relatively acellular hemolymph has a viscosity that is similar to acellular human plasma at a comparable shear rate [~2.5 centipoise (Rand et al., 1964)], we estimated intracardiac shear stress of ~1-2 dyne/cm^2, which is similar to the intracardiac shear stress present in a 37 h.p.f. zebrafish embryo (Hove et al., 2003).

Systolic and diastolic heart wall dysfunction demonstrated using Doppler heart wall velocimetry of normal and *hdp2* mutant hearts

It is evident from Fig. 2 that M-mode Doppler OCT is sensitive to Doppler shifts generated by heart wall motion. We exploited this sensitivity to perform tissue Doppler-imaging-based heart wall velocimetry (Fig. 3), in analogy with clinical, ultrasound-based tissue Doppler imaging of human heart wall velocities (Ho and Solomon, 2006; Marcucci et al., 2008). As shown in Table 1 and Fig. 4, we demonstrated that the *hdp2* mutants have a statistically significant slower peak systolic and diastolic ventral wall velocity compared with OreR wild-type hearts. Thus, just as human hearts can demonstrate dysfunction beyond pump efficiency, mutant *D. melanogaster* hearts can have homologous physiological dysfunction that is evident only through sophisticated biomechanical phenotyping.

In contrast to prior research demonstrating a dilated phenotype in adult *hdp2* mutants (Wolf et al., 2006), our results indicate that the pre-pupal *hdp2* heart is not dilated (Table 1). Similarly to the adult *hdp2* heart (Wolf et al., 2006), the pre-pupal *hdp2* heart has depressed systolic function as assessed with fractional shortening. However, compared with the wild-type OreR pre-pupa, the *hdp2* fractional shortening is only mildly depressed (73% versus 66%). However, the differences in systolic ventral wall velocities, another measure of systolic function, are large (730 μm/second versus 532 μm/second). To compare shortening fraction and systolic wall velocity as diagnostic tests, we generated receiver operator characteristic (ROC) curves (Hanley and McNeil, 1982; Zou et al., 2007) for each measure (Fig. 4). Since each ROC curve is well above the 45° line (i.e. sensitivity=[1−specificity]), each is a useful discriminator of mutant and wild-type genotypes. However, systolic wall velocity had an area under the curve of 0.85±0.066 (mean ± s.e.) and fractional shortening had an area under the curve of 0.62±0.097, indicating that systolic wall velocity is a stronger discriminator.

Aortic physiology

Our focused imaging of the aorta during the cardiac cycle revealed aortic wall behavior that is different from that of the human aorta. In humans, the diameter of the aorta is not critically sensitive to variation in intraluminal pressures during the cardiac cycle. Using OCT, we showed that the pre-pupal *D. melanogaster* has an aortic diameter that is cardiac-cycle dependent. During diastole, the aorta

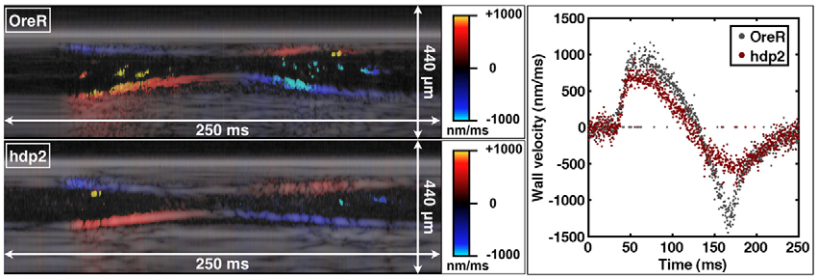

Fig. 3. M-mode OCT-based tissue Doppler imaging of wild-type and mutant heart wall velocity. The left panels are representative M-mode images of OreR and *hdp2* hearts during systole and diastole. The right panel is a plot of the wall velocity as a function of time, taken along a linear region of interest on the ventral wall. The occasional zero-valued datapoints are Doppler pixels on the linear region of interest that are rejected based on the intensity of the corresponding structural pixel.

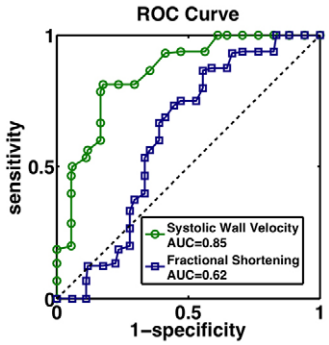

Fig. 4. Receiver-operator characteristic (ROC) curves for two measures of systolic heart function: fractional shortening (blue squares) and ventral wall systolic wall peak velocity (green circles). The dashed black line is the 45° line. AUC, area under the curve.

collapses and, during systole, the aortic diameter considerably increases (Fig. 5; supplementary material Movies 5 and 6). The systolic increase in diameter occurs in a posterior-to-anterior direction away from the heart towards the head, consistent with the transmission of a pressure wave from the contracting heart down the aorta towards the head. As systole ends, the aorta collapses in a posterior-to-anterior direction. The absence of aortic dye during diastole is also consistent with a time-varying diameter that is at its minimum during diastole.

We used dye angiography and digital subtraction angiography to image aortic flow dynamics. This imaging showed the rapid transport of a bolus of fluid ejected from the heart, through the aorta, and into the extracellular-extravascular space in the head (Fig. 6; supplementary material Movie 7). The time-varying diameter of the aortic lumen was also evident from dye angiography movies. Using this imaging we calculated aortic velocities ranging from 1.40 to 2.55 body lengths per second (n=5 organisms; mean ± s.d., 1.79±0.46). These velocities are consistent with vertebrate intracardiac flow velocities. For comparison, peak human aortic velocity is on the order of 1.0-1.7 m/second (DeMaria and Blanchard, 2007), which corresponds to ~1 body length per second. In dog, peak aortic velocity is ~1.5 body length per second (Wallmeyer et al., 1986), assuming a body length of ~1 m; in mouse, ~4 body lengths per second (Greve et al., 2006) assuming a body length of 9 cm (Vitarius et al., 2006); in 2 d.p.f. zebrafish embryos, ~1 body length per second assuming a body length of ~3.5 mm (Muller and van Leeuwen, 2004); and in 5 d.p.f. zebrafish embryos, ~1 body length per second assuming a body length of ~4 mm (Schilling, 2002).

Extracellular-extravascular flow dynamics and mass transport

We used dye angiography in the *D. melanogaster* pre-pupa to gain insight into global flow dynamics and extracellular-extravascular flow dynamics (Figs 1 and 6; supplementary material Movies 2-4, 8-9). Transport of dye away from an injection site was driven by cardiac cycle-dependent convective transport. Fig. 1I demonstrates very little diffusion of dye in an anterior direction away from the injection site. There also was convective transport of dye anterior to the injection only after dye accumulation at the head, suggesting that cardiac-cycle-driven convection can dominate over diffusion. Put another way, the cardiac transport of dye from the heart to the head towards the injection was more efficient that diffusion driven by local concentration gradients. The dependence of mass transport on the cardiac cycle was most evident upon resumption of the cardiac cycle following a period of asystole that occasionally occurs after puncture of the cuticle and injection of dye (Fig. 6; supplementary material Movie 8). During asystole, there was little transport of dye away from the injection site, despite a strong concentration gradient that favors diffusion. Upon resumption of the cardiac cycle, transport of dye away from the injection site was rapid. These findings support the hypothesis that convection has a central role in bulk mass transport in the pre-pupal *D. melanogaster*.

Dye angiography also provided evidence for fast, non-isotropic, extracellular-extravascular, cardiac-cycle-dependent mass transport. Dye injected far from the heart tube returned to the heart via preferred flow channels, despite the absence of discrete return vessels (Fig. 6; supplementary material Movies 8, 9). One of these channels is adjacent to the large tracheal tubes present on either side of the pre-pupae. Another one of these channels is dorsal to the aorta itself. The existence of a dorsal return channel was supported by our OCT imaging of the aorta that showed an anterior-to-posterior stream of hemocytes dorsal to the aorta (supplementary material Movie 5).

DISCUSSION

The results presented here advance the study of the open cardiovascular system of *D. melanogaster* and support its use as an animal model of complex human cardiovascular disease. We demonstrated physiological homology between the pre-pupal *D. melanogaster* and vertebrate cardiovascular systems. This conclusion is supported by (1) similarities in heart performance measures, (2) similar rates of flow in the great vessels, (3) the presence of cardiac-dependent, convection-limited bulk mass transport, (4) non-isotropic return flow to the heart, and (5) the existence of complex functional heart defects that are evident only through detailed functional characterization.

Table 1. *hdp2* hearts have normal fractional shortening but diminished systolic and diastolic wall velocities compared with wild-type pre-pupal hearts

	n	Systolic wall velocity (μm/second)	Diastolic wall velocity (μm/second)	EDD (μm)	ESD (μm)	FS (%)
OreR wild type	18	730±37	511±35	134±4.6	37±4.9	73±3.3
hdp2	16	532±39	393±25	136±4.5	47±3.3	66±2.2
P value		0.00043*	0.0049*	0.39	0.061	0.047*

Values are reported as mean ± s.e.m. *P* values are from one-tailed, heteroscedastic *t*-tests. Statistically significant differences (P<0.05) are indicated with an asterisk. EDD, end-diastolic diameter; ESD, end-systolic diameter; FS, fractional shortening.

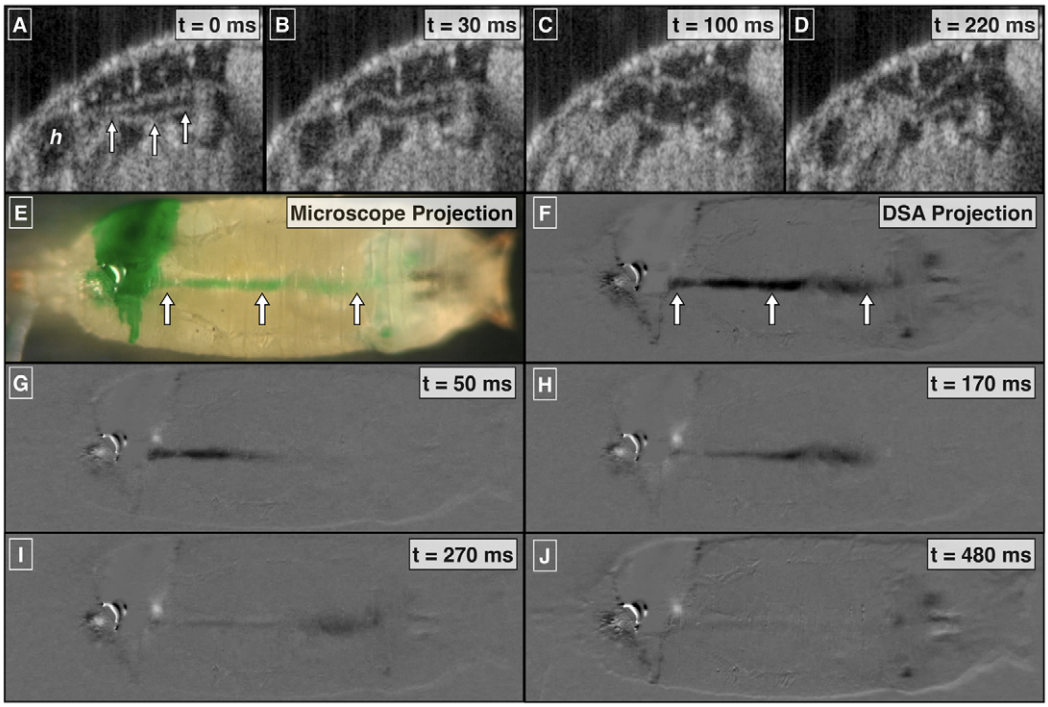

Fig. 5. Focused imaging of aortic flow and wall dynamics. Structural OCT (A-D; supplementary material Movie 5), dye angiography (E; supplementary material Movie 7) and digital subtraction angiography (DSA) (F-J; supplementary material Movie 7). Arrows indicate the aorta. Projection images, taken over 500 milliseconds, clearly outline the course of the aorta and show dye that is delivered to the head over the course of the cardiac cycle. Still frames from the DSA movie clearly show bolus-like transport of dye through the aorta. h, heart.

The wild-type pre-pupal *D. melanogaster* has vigorous, cardiac-cycle-dependent convective mass transport that can transport a nanoliter-scale stroke volume an entire body length within a few hundred milliseconds. Of particular note, we identified four vigorous flow streams along the anterior-posterior axis, the longest dimension of the organism. One stream has a posterior-to-anterior direction (aortic flow), whereas the other three streams (two para-tracheal streams and one stream dorsal to the aorta) have an anterior-to-posterior direction. The presence of vigorous, anti-parallel flow streams along the longest dimension of the animal suggests a fairly well organized flow circuit across distances that are prohibitively difficult for diffusion to traverse. Moreover, weight-adjusted cardiac output and other physiological measures are similar to those in humans. Just as diffusion has a role in mass transport from the vascular to the extracellular-extravascular compartment in vertebrates (Boulpaep, 2008), the present study does not exclude the role of diffusion over small spatial scales in the *D. melanogaster* extracellular-extravascular space. However, the presence of vigorous intravascular and extracellular-extravascular flow should dramatically increase diffusion rates over those spatial scales by maintaining a relatively constant 'source' for diffusion-mediated delivery and a 'sink' for diffusion-mediated removal.

Although our results support physiological homology between *D. melanogaster* and vertebrate cardiovascular systems, aortic wall imaging did highlight a difference between the *D. melanogaster* aorta and vertebrate aortas: the pre-pupal *D. melanogaster* aortic diameter varies dramatically during the cardiac cycle, whereas vertebrate aortic diameters tend to be relatively constant throughout the cardiac cycle. Previous aortic imaging was limited in its ability to assess the dynamic behavior characterized by OCT. The time-varying diameter of the aorta is predominantly manifest along its superior-inferior axis. This spatial dimension is difficult to assess through en face cross-sectional imaging (e.g. confocal microscopy) and through traditional widefield microscopy (which essentially produces a projection image over the depth of field along the superior-inferior axis). In addition, the pressure-sensitive opening and collapse of the aorta during the cardiac cycle is not immediately obvious from prior histological and anatomical studies. Similarly to the heart itself, the aorta is composed of two layers, each of which is one cell thick: an inner layer of myocardial cells and an outer layer or pericardial cells (Small and Krieg, 2002). The myocardial cells of both the heart and aorta contain muscle-specific markers such as polymerized actin (Lo et al., 2002), muscle myosin heavy chain (Lovato et al., 2002) and heart-specific markers such as myocyte enhancer factor-2 (Lovato et al., 2002). Even though the heart and aorta are both composed of myocytes, there is growing evidence that subdifferentiation of myocytes into the heart and aorta is driven by distinct genetic programs (Lo et al., 2002). This subdifferentiation appears to have a physiological correlate: the heart acts as a pulsatile, contractile fluid pump whereas the aorta acts as a non-pumping vessel with a pressure-dependent diameter.

Furthermore, the pressure-sensitive behavior of the pre-pupal *D. melanogaster* aorta shares features with the phenomenon of

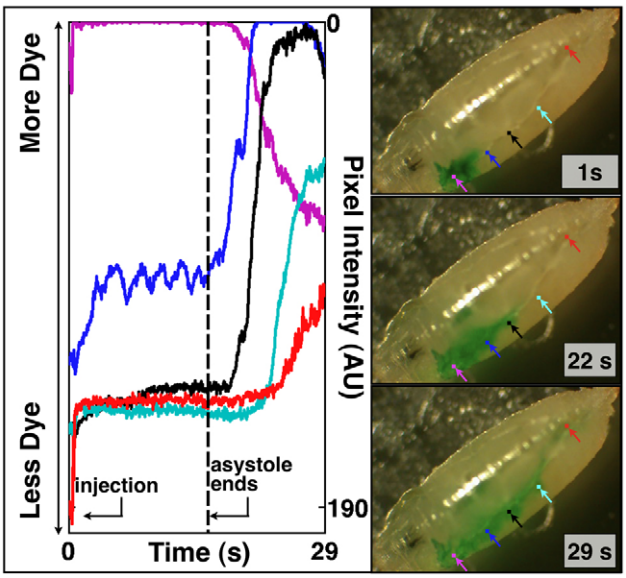

Fig. 6. Injection near the head demonstrates preferential return flow that is dependent upon the cardiac cycle. After injection, the heart enters a ~16 second period of asystole. During asystole, there is little transport of dye away from the injection site. This is evident from time-varying plots of local pixel intensity. The small oscillations around baseline at the blue-dot region of interest are probably secondary to head motion (see supplementary material Movie 8). Resumption of the cardiac cycle initiates anterior-to-posterior return flow to the heart. The flow is preferentially along the trachea and dorsal to the aorta.

critical closing pressure. Critical closing pressure refers to microvascular collapse secondary to steady-state active muscular vascular tension in the presence of vascular elasticity (Nichol et al., 1951). Collapse can be overcome by a threshold pressure that is determined by the degree of active wall tension and vessel wall elasticity. Given that the aorta contain cells of myocardial origin and actively express muscle-specific markers, it is possible that these cells generate the active tension necessary for clinical closing pressure. The existence of threshold behavior dictates that a vessel governed by critical closing pressure has a hemodynamic resistance that decreases dramatically in the face of a threshold forward (i.e. posterior to anterior) pressure. Of note, valves obey a similar nonlinear rule. That is, in the face of a certain threshold forward pressure, the resistance across a valve decreases dramatically. Although a vessel governed by critical closing pressure is insensitive to the direction of an applied pressure wave, in pre-pupal *D. melanogaster* there is no apparent mechanism to generate a backward (i.e. anterior to posterior) pressure. Thus, the aorta itself appears to have valve-like properties.

Ultrasound-based Doppler heart wall velocimetry in humans is an increasingly important imaging modality in the biomechanical characterization of failing hearts (Ho and Solomon, 2006; Marcucci et al., 2008; Maeder and Kaye, 2009). One important clinical insight from sophisticated clinical imaging techniques is that functional defects exist beyond pump efficiency (e.g. fractional shortening, ejection fraction). Our results using OCT-based Doppler heart wall velocimetry show impaired systolic and diastolic heart wall velocities in the *hdp2* troponin I mutant, arguing for physiological homology in heart dysfunction and failure. ROC curve analysis suggests that, in the setting of a genotype with borderline changes in structural echocardiographic parameters (e.g. chamber diameters), defects in systolic function may be more readily identified by Doppler wall velocimetry. OCT-based tissue Doppler imaging also opens up possibilities to specifically study diastolic dysfunction in the *D. melanogaster* animal model of human heart failure. Likewise, by focusing primarily on global physiological characterization, several cardiovascular phenotypes have been identified (e.g. weight-adjusted cardiac output, intracardiac shear forces, aortic flow velocity) that can form the basis for future studies, such as the role of biomechanical forces in *D. melanogaster* heart development.

METHODS

D. melanogaster culture and pre-pupal selection

OreR and *hdp2 D. melanogaster* were raised on reconstituted dry medium (Carolina Biological Supply, Burlington, NC) and were exposed to ambient light-dark cycles. Files were cultured and imaged at 24°C. Pre-pupae, in contradistinction to late third instar wandering larvae, were defined as (1) being stationary, (2) having a lack of whole body motion, (3) being unresponsive to gentle touch stimuli, (4) having a cuticle, as ascertained by gently pushing on the animal with a blunt instrument, (5) being untanned in white light illumination. Before imaging, pre-pupae were carefully washed with a normal saline solution and dried with the gentle application of tissue paper.

Structural and Doppler optical coherence tomography (OCT) imaging

Two OCT systems were used. Baseline structural and Doppler characterization of OreR hearts (Figs 1, 2, 3, 5 and echocardiographic parameters in the "Cardiac physiology" subsection) was performed using a custom-built 1300 nm OCT system with A-line rates of 10 or 20 kHz (Vakoc et al., 2005). Quantitative comparisons of OreR and *hdp2* hearts (Table 1 and Fig. 4) were made using a commercially available OCT system (Thorlabs, Newton, NJ) with a 1325 nm center wavelength and an A-line rate of 16 kHz. Post-processing and chamber measurements were performed using MATLAB (Mathworks, Natick, MA) and ImageJ (Wayne Rasband, National Institutes of Health, Bethesda, MD). End systolic and diastolic diameters for an individual specimen were reported as the average diameters measured for two distinct heartbeats. Fractional shortening was calculated as (EDD–ESD)/EDD. Fractional shortening for an individual specimen were reported as the average of fractional shortening measurements made on two distinct heart heats and not from average values of EDD and ESD.

For Doppler imaging, conversion from measured Doppler shift (f_d) to velocity (v) used the standard Doppler equation for echo-based Doppler velocimetry ($f_d=2v\cos(\theta)n\nu/c$; θ, Doppler angle; n, tissue optical index; ν, optical frequency; c, free-space vacuum speed of light). For Doppler imaging of hemocyte velocity, a Doppler angle of 65° was assumed based on end-diastolic geometry of the heart during sagittal plane imaging. For Figs 2 and 3 the background Doppler signal was thresholded based on the structural M-mode image. OCT-based tissue Doppler wall velocimetry used a semi-automated processing algorithm. M-mode Doppler data,

processed using the Kasai algorithm (Mariampillai et al., 2007) with a 1 millisecond × 5.7 μm window, was displayed using standard Doppler color maps in ImageJ. The area of subjective maximum systolic wall velocity for a particular beat was estimated by drawing a 2 millisecond × 5.7 μm region of interest and calculating the mean Doppler signal over that region of interest. This measurement was performed for two systolic beats for each M-mode recording. It was assumed that wall motions were parallel to the optical axis (i.e. Doppler angle of 0°). One-sided, unpaired, heteroscedastic *t*-tests were used to compare mean heart wall velocities between OreR and *hdp2* hearts. The assumption of heteroscedasticity was based on *F*-test values of <95% for all comparisons.

Receiver-operator characteristic (ROC) curve statistics

ROC curves were generated using a non-parametric approach (Zou et al., 2007) with custom MATLAB scripts. For a given measure of systolic performance (i.e. either fractional shortening or systolic wall velocity), a data array was generated that represented the sorted values across both genotypes (i.e. OreR and *hdp2*). The array had 34 elements, representing the combined sample size (16 *hdp2* and 18 OreR samples). Sensitivity and specificity datapoints were calculated using each element of this array as a cut-off value. A true positive (negative) was defined as an OreR (*hdp2*) measurement being larger than (less than) a given cut-off value. ROC curves were plotted using these 34 estimates of sensitivity and specificity. Area under the curve (AUC) and standard error of AUC was calculated as per Hanley and McNeil (Hanley and McNeil, 1982).

Dye angiography

The microinjection system used pressurized nitrogen, a pressure controller, and custom-pulled micropipettes. Glass capillary tubes were pulled with a vertical pipette puller. The tapered ends were manually broken to create a jagged, sharp end with an outer diameter between ~50-150 micrometers. The micropipette was connected to the microinjection system and was filled with green dye (water, propylene glycol, FD&C yellow 5, FD&C blue 1, propylparaben; McCormick, Sparks, MD) via application of negative pressure. The cuticle was punctured by the micropipette. If needed, after initial puncture, the micropipette was withdrawn to eject any hemolymph that, via diffusion and capillary effect, had mixed with the dye. Dye was introduced by a few brief (30-60 milliseconds) pressure bursts at 3-6 p.s.i. Dye angiography movies were recorded at 320 (vertical) × 240 (horizontal) pixel resolution at 15 frames per second (f.p.s.) or with high definition 1080i (1920 vertical × 1080 horizontal) pixel resolution at an interlaced frame rate of 29.97 f.p.s. using a Nikon CoolPix 995 camera or a Sony HDR-HC9 camcorder, respectively. The camera was mounted to the trinocular port of an Olympus SZ-H10 stereomicroscope.

Dye angiography image analysis and digital subtraction angiography

After dye angiography sessions, digital microscopy movies were transferred to a personal computer (MacBook Pro, Apple, Inc, Cupertino, CA) and analyzed using ImageJ and MATLAB. For time-varying pixel intensity measurements, the red channel of the RGB image was used. The red channel showed the most contrast between dye and the surrounding tissue. Time-varying pixel intensity plots were generated by (1) loading the red channel of a dye angiography movie into ImageJ as an image stack, (2) selecting a square region of interest (ROI), and (3) using the 'Plot Z-axis Profile' tool to generate the average pixel intensity within the ROI for each image in the stack. For aortic velocity measurements, the time-varying pixel intensity was acquired for a proximal and distal ROI on the aorta. As the dye bolus traverses past each ROI, the pixel intensity drops to a maximum and then return to baseline. The number of frames between the pixel intensity minimum for each ROI was counted. Dye velocity was calculated using this time delay and the measured distance between the two ROIs. Each reported velocity is the average of three such measurements for an individual animal.

Digital subtraction angiography (DSA) was performed in ImageJ using deinterlaced HVD 1080i movies that have a native interlaced frame rate of 29.97 f.p.s. The deinterlaced movie frame rate was 59.94 f.p.s. The red color channel was used for DSA processing. For the images and movies shown in this manuscript, the background image was based on the arithmetic mean image from the 56 frames before onset of systole. Using the image calculator in ImageJ, this background image was subtracted from the subsequent 60 frames.

TRANSLATIONAL IMPACT

Clinical issue

Advances in our understanding and treatment of heart failure have been underpinned by detailed physiological characterization of normal and failing hearts. Physiological characterization has also shown that measures such as heart wall velocity, when combined with traditional measures of heart pump efficiency (e.g. fractional shortening, ejection fraction), are important for diagnosing and classifying heart failure. The importance of subtle and robust characterization raises two important questions regarding the use of *Drosophila melanogaster* as an animal model of human heart failure. First, are baseline measures of cardiovascular physiology similar between vertebrates and *D. melanogaster*? Second, can subtle defects in heart function be demonstrated in *D. melanogaster* hearts?

Results

Using optical imaging techniques, the authors show that baseline measures of cardiovascular physiology in pre-pupal *D. melanogaster* are similar to those in vertebrates. Comparisons made on the basis of normalized measures (e.g. weight-adjusted cardiac output, body-length-adjusted aortic flow velocities) suggest there is physiological homology in normal functioning. Using Doppler optical coherence tomography (the optical analogue of ultrasound Doppler imaging), the authors show that the troponin mutant *hdp2* has a pre-pupal heart with impaired systolic and diastolic wall velocities with only mildly depressed fractional shortening. As troponin mutations are a cause of familial heart disorders in humans, the presence of subtle functional defects as well as quantitative diastolic dysfunction in *hdp2* flies suggests homology in heart dysfunction between *D. melanogaster* and humans.

Implications and future directions

The similarities observed here between vertebrate and *D. melanogaster* cardiovascular systems support the use of *D. melanogaster* as an animal model of complex cardiovascular disease. Optical imaging in the partially transparent pre-pupa, allowing quantification of physiological performance, will be a robust basis for future studies in mutant *D. melanogaster* hearts. This technique will also provide a basis for identifying genotype-phenotype relationships that might yield insight into complex clinical disease states such as diastolic heart dysfunction and heart failure with normal left ventricular ejection fraction.

Deinterlacing of 1080i video

Deinterlacing was performed using custom MATLAB code that assigned odd and even numbered lines in a frame to sequential odd and even frames, respectively. To maintain the aspect ratio and pixel density of the deinterlaced frame, each line i from the native interlaced frame served as lines i and i+1 if i was odd and as lines i–1 and i if i was even. This non-motion-compensated, linear-deinterlacing method is called line repetition (De Haan and Bellers, 1998). The jitter of stationary objects is a well-recognized artifact of this deinterlacing technique.

Movie compression

All movies were compressed using MPEG-4 compression in QuickTime Pro (Apple, Cupertino, CA).

ACKNOWLEDGEMENTS

This work was generously supported by the Frederick H. Lovejoy Fund, Children's Hospital Boston (M.A.C.) and by an American Medical Association Foundation Seed Grant (M.A.C.). We additionally acknowledge funding support from NIH R01HL076398 and NIH R01CA103769 (development of the imaging system) and from the Department of Defense Air Force Office of Scientific Research, Medical Free Electron Laser Program FA9550-04-1-0079. We thank Thorlabs their loan of an OCT system. We thank James Vigoreaux for supplying *hdp2 D. melanogaster*.

AUTHOR CONTRIBUTIONS

M.A.C. conceived, designed and conducted the experiments, performed the data analysis and wrote the manuscript. G.J.T. contributed to experimental design. B.J.V., B.E.B. and G.J.T. designed the custom OCT system and software and M.J.S. built the custom OCT system. B.J.V. and M.J.S. provided technical support. B.E.B. and G.J.T. supervised the research. All authors edited and reviewed the final manuscript.

SUPPLEMENTARY MATERIAL

Supplementary material for this article is available at
http://dmm.biologists.org/lookup/suppl/doi:10.1242/dmm.005231/-/DC1

REFERENCES

Beall, C. J. and Fyrberg, E. (1991). Muscle abnormalities in drosophila-melanogaster heldup mutants are caused by missing or aberrant troponin-I isoforms. *J. Cell Biol.* **114**, 941-951.

Berne, R. M. and Levy, M. N. (1950). Effects of acute reduction of cardiac output on the renal circulation of the dog. *J. Clin. Investig.* **29**, 444-454.

Bier, E. and Bodmer, R. (2004). Drosophila, an emerging model for cardiac disease. *Gene* **342**, 1-11.

Birchard, G. F. and Arendse, A. U. (2001). An allometric analysis of oxygen consumption rate and cardiovascular function in the cockroach, Blaberus discoidalis. *Comp. Biochem. Physiol. A Mol. Integr. Physiol.* **129**, 339-344.

Boulpaep, E. L. (2008). Organization of the cardiovascular system. In *Medical Physiology* (ed. W. F. Boron and E. L. Boulpaep), pp. 430. New York: Saunders.

Choma, M. A., Izatt, S. D., Wessells, R. J., Bodmer, R. and Izatt, J. A. (2006). In vivo imaging of the adult Drosophila melanogaster heart with real-time optical coherence tomography. *Circulation* **114**, E35-E36.

Curtis, N. J., Ringo, J. M. and Dowse, H. B. (1999). Morphology of the pupal heart, adult heart, and associated tissues in the fruit fly, Drosophila melanogaster. *J. Morphol.* **240**, 225-235.

De Haan, G. and Bellers, E. B. (1998). Deinterlacing-an overview. *Proc. IEEE* **86**, 1839-1857.

DeMaria, A. N. and Blanchard, D. G. (2007). Echocardiography. In *Hurst's The Heart* (ed. V. Fuster, R. A. O'Rourke, R. A. Walsh and P. Poole-Wilson). http://www.accessmedicine.com/content.aspx?aID=3063939.

Folk, D. G., Han, C. and Bradley, T. J. (2001). Water acquisition and partitioning in Drosophila melanogaster: effects of selection for desiccation-resistance. *J. Exp. Biol.* **204**, 3323-3331.

Greve, J. M., Les, A. S., Tang, B. T., Draney Blomme, M. T., Wilson, N. M., Dalman, R. L., Pelc, N. J. and Taylor, C. A. (2006). Allometric scaling of wall shear stress from mice to humans: quantification using cine phase-contrast MRI and computational fluid dynamics. *Am. J. Physiol. Heart Circ. Physiol.* **291**, H1700-H1708.

Hanley, J. A. and McNeil, B. J. (1982). The meaning and use of the area under a receiver operating characteristic (ROC) curve. *Radiology* **143**, 29-36.

Ho, C. Y. and Solomon, S. D. (2006). A clinician's guide to tissue Doppler imaging. *Circulation* **113**, e396-e398.

Hove, J. R., Koster, R. W., Forouhar, A. S., Acevedo-Bolton, G., Fraser, S. E. and Gharib, M. (2003). Intracardiac fluid forces are an essential epigenetic factor for embryonic cardiogenesis. *Nature* **421**, 172-177.

Hu, N., Sedmera, D., Yost, H. J. and Clark, E. B. (2000). Structure and function of the developing zebrafish heart. *Anat. Rec.* **260**, 148-157.

Huang, D., Swanson, E. A., Lin, C. P., Schuman, J. S., Stinson, W. G., Chang, W., Hee, M. R., Flotte, T., Gregory, K., Puliafito, C. A. et al. (1991). Optical coherence tomography. *Science* **254**, 1178-1181.

Janssen, B., Debets, J., Leenders, P. and Smits, J. (2002). Chronic measurement of cardiac output in conscious mice. *Am. J. Physiol.* **282**, R928-R935.

Kern, M. J. and King, S. B. I. (2008). Cardiac catheterization, cardiac angiography, and coronary blood flow and pressure measurements. In *Hurst's The Heart* (ed. V. Fuster, R. A. O'Rourke, R. A. Walsh and P. Poole-Wilson). http://www.accessmedicine.com/content.aspx?aID=3058540.

Kirby, M. L. and Schachat, F. (2007). Evolutionary developmental biology of the heart. In *Cardiac Development* (ed. M. L. Kirby), pp. 199-214. New York: Oxford University Press.

Kuczmarski, R. J., Ogden, C. L., Grummer-Strawn, L. M., Flegal, K. M., Guo, S. S., Wei, R., Mei, Z., Curtin, L. R., Roche, A. F. and Johnson, C. L. (2000). CDC growth charts: United States. *Adv. Data*, **314**, 1-27.

Lang, R. M., Bierig, M., Devereux, R. B., Flachskampf, F. A., Foster, E., Pellikka, P. A., Picard, M. H., Roman, M. J., Seward, J., Shanewise, J. S. et al. (2005). Recommendations for chamber quantification: a report from the American Society of Echocardiography's Guidelines and Standards Committee and the Chamber Quantification Writing Group, developed in conjunction with the European Association of Echocardiography, a branch of the European Society of Cardiology. *J. Am. Soc. Echocardiogr.* **18**, 1440-1463.

Lo, P. C. H., Skeath, J. B., Gajewski, K., Schulz, R. A. and Frasch, M. (2002). Homeotic genes autonomously specify the anteroposterior subdivision of the Drosophila dorsal vessel into aorta and heart. *Dev. Biol.* **251**, 307-319.

Lock, J. E. (2006). Cardiac catheterization. In *Nadas' Pediatric Cardiology* (ed. J. F. Keane, J. E. Lock and D. C. Fyler). New York: Elsevier.

Lovato, T. L., Nguyen, T. P., Molina, M. R. and Cripps, R. M. (2002). The Hox gene abdominal-A specifies heart cell fate in the Drosophila dorsal vessel. *Development* **129**, 5019-5027.

Maeder, M. T. and Kaye, D. M. (2009). Heart failure with normal left ventricular ejection fraction. *J. Am. Coll. Cardiol.* **53**, 905-918.

Malone, M. H., Sciaky, N., Stalheim, L., Hahn, K. M., Linney, E. and Johnson, G. L. (2007). Laser-scanning velocimetry: a confocal microscopy method for quantitative measurement of cardiovascular performance in zebrafish embryos and larvae. *BMC Biotechnol.* **7**, 40.

Marcucci, C., Lauer, R. and Mahajan, A. (2008). New echocardiographic techniques for evaluating left ventricular myocardial function. *Semin. Cardiothorac. Vasc. Anesth.* **12**, 228-247.

Mariampillai, A., Standish, B. A., Munce, N. R., Randall, C., Liu, G., Jiang, J. Y., Cable, A. E., Vitkin, I. A. and Yang, V. X. D. (2007). Doppler optical cardiogram gated 2D color flow imaging at 1000 fps and 4D in vivo visualization of embryonic heart at 45 fps on a swept source OCT system. *Optics Express* **15**, 1627-1638.

Mohrman, D. E. and Heller, L. J. (2006). *Cardiovascular Physiology.* New York: McGraw-Hill.

Muller, U. K. and van Leeuwen, J. L. (2004). Swimming of larval zebrafish: ontogeny of body waves and implications for locomotory development. *J. Exp. Biol.* **207**, 853-868.

Nichol, J., Girling, F., Jerrard, W., Claxton, E. B. and Burton, A. C. (1951). Fundamental instability of the small blood vessels and critical closing pressures in vascular beds. *Am. J. Physiol.* **164**, 330-344.

Papanastasiou, T. C., Georgiou, G. C. and Alexandrou, A. N. (2000). *Unidirectional Flows.* New York: CRC Press.

Pistner, A., Belmonte, S., Coulthard, T. and Blaxall, B. (2010). Murine echocardiography and ultrasound imaging. *J. Vis. Exp.* **Pii**, 2100.

Rand, P. W., Lacombe, E., Hunt, H. E. and Austin, W. H. (1964). Viscosity of normal human blood under normothermic and hypothermic conditions. *J. Appl. Physiol.* **19**, 117-122.

Roy, S., Gnyawali, S. C., Driggs, J., Khanna, S., Ryan, T. and Sen, C. K. (2010). High-frequency high-resolution echocardiography: first evidence on non-invasive repeated measure of myocardial strain, contractility, and mitral regurgitation in the ischemia-reperfused murine heart. *J. Vis. Exp.* **Pii**, 1781.

Schilling, T. F. (2002). The morphology of larval and adult zebrafish. In *Zebrafish: A Practical Approach* (ed. C. Nüsslein-Volhard and R. Dahm), pp. 59-94. New York: Oxford University Press.

Slama, M., Susic, D., Varagic, J., Ahn, J. and Frohlich, E. D. (2003). Echocardiographic measurement of cardiac output in rats. *Am. J. Physiol. Heart Circ. Physiol.* **284**, H691-H697.

Small, E. M. and Krieg, P. A. (2002). Molecular mechanisms of chamber-specific myocardial gene expression: transgenic analysis of the ANF promoter. In *The Cardiovascular System (Cold Spring Harbor Symposia on Quantitative Biology)*, pp. 71-80. Woodbury, New York: Cold Spring Harbor Laboratory Press.

Squires, T. M. and Quake, S. R. (2005). Microfluidics: Fluid physics at the nanoliter scale. *Rev. Mod. Phys.* **77**, 977-1026.

Vakoc, B. J., Yun, S. H., de Boer, J. F., Tearney, G. J. and Bouma, B. E. (2005). Phase-resolved optical frequency domain imaging. *Optics Express* **13**, 5483-5493.

Vitarius, J. A., Sehayek, E. and Breslow, J. L. (2006). Identification of quantitative trait loci affecting body composition in a mouse intercross. *Proc. Natl. Acad. Sci. USA* **103**, 19860-19865.

Vogel, S. (1993). *Vital Circuits.* New York: Oxford University Press.

Wallmeyer, K., Wann, L. S., Sagar, K. B., Kalbfleisch, J. and Klopfenstein, H. S. (1986). The influence of preload and heart rate on Doppler echocardiographic indexes of left ventricular performance: comparison with invasive indexes in an experimental preparation. *Circulation* **74**, 181-186.

Wolf, M. J., Amrein, H., Izatt, J. A., Choma, M. A., Reedy, M. C. and Rockman, H. A. (2006). Drosophila as a model for the identification of genes causing adult human heart disease. *Proc. Natl. Acad. Sci. USA* **103**, 1394-1399.

Yip, G., Abraham, T., Belohlavek, M. and Khandheria, B. K. (2003). Clinical applications of strain rate imaging. *J. Am. Soc. Echocardiogr.* **16**, 1334-1342.

Zou, K. H., O'Malley, A. J. and Mauri, L. (2007). Receiver-operating characteristic analysis for evaluating diagnostic tests and predictive models. *Circulation* **115**, 654-657.